

4D Pixel Mechanical Metamaterials with Programmable and Reconfigurable Properties

Xiaozhou Xin, Liwu Liu,* Yanju Liu, and Jinsong Leng*

The tension-torsion coupling metamaterial (TTCM) exhibits torsional deformation while stretching, with the degree of freedom exceeding the Cauchy elasticity. However, the TTCM suffers from the limitations of the weak tension-torsion coupling effect (TTCE), narrow deformation domain, and lack of adaptability. To address these limitations, mechanical pixel (MP) array design, helical microstructure, and 4D printing are introduced into the TTCM in this study, providing new strategies to exploit the deformation potential of the TTCM. The developed MP exhibits the tunability, programmability, and reconfigurability of the mechanical behaviors (stress–strain relationship, TTCE). The pixel mechanical metamaterial (PMM) with uncoupled deformation between MPs is obtained, which greatly enriches the design diversity of configurations and maintainability. The application prospects of the developed PMM for information encryptions, kinematics controllers, soft robots, and buffer devices are demonstrated. More interestingly, an egg falling on the PMM at the height of ≈ 1 m remains intact due to the excellent protection performance of the PMM.

1. Introduction

Mechanical metamaterials are artificial materials consisting of periodic optimized microstructures, which gain their extraordinary mechanical properties from structure rather than composition, such as auxetic behavior, negative thermal expansion, negative stiffness, and reconfigurability, etc.^[1–16] These unusual mechanical properties enable mechanical metamaterials to be developed into flexible electronics and soft robots with novel functions and innovative applications, such as flexible electronics that match tissue deformation and buckling-driven soft mechanisms.^[4,6,17–19] The tension-torsion coupling metamaterial (TTCM), as a typical mechanical metamaterial, exhibits torsional deformation when subjected to a tensile/compressive load (i.e., force–torque coupling), with degree of freedom (DOF)


exceeding the Cauchy elasticity.^[20–24] Generally, the TTCM consists of periodically interconnected microstructures that maintain the inherent configuration and exhibit macroscopic constitutive behavior. However, the interconnected microstructures are mutually restricted and highly coupled in kinematics, limiting the potential deformation and reducing the reusability and maintainability of the metamaterials.^[25] Additionally, the mechanical properties (stress–strain σ – ε relationship, torsion angle φ) of the TTCM are controlled by the configuration of the microstructures, meaning that the mechanical properties of the TTCM are fixed and irreversible after fabrication. As a result, the following three major limitations of TTCMs greatly restrict the applications of TTCMs: i) weak tension-torsion coupling effects (TTCE, $\varphi/\varepsilon \approx 0.2$ rad $\%^{-1}$),^[26] ii) narrow deformation domain (especially tensile strain), and iii) non-programmable mechanical behaviors after fabrication.

To break through these limitations of the TTCM, in this work, we proposed a novel strategy combining bio-inspired design and 4D printing. Hedgehog spines can be used to threaten and stab predators, and can also effectively buffer the impact when falling from a height of ≈ 10 m. Since the spines are not connected to each other, the damage of one spine will not affect the other spines, thereby effectively preventing further damage.^[49,50] Inspired by the array mode of hedgehog spines, the pixel mechanical metamaterial (PMM) was developed by the array of uncoupled constrained individuals (i.e., mechanical pixel, MP), which exhibited a great degree of design freedom, modularity, and diversity of configuration/mechanical properties.^[25,49,50] Similar to screen-adjusted 2D images by changing the color of the pixels, the PMM adjusted mechanical properties by changing the configuration of the MP.^[1,25] The helix-shaped collagen fibers in the biological tissue (such as skin) undergo the deformation mode from the bending-dominant to the stretching-dominant.^[17,51] This transformation of deformation mode enable it to exhibit a J-shaped stress-strain curve, which provides an opportunity for the design of structures with large deformation capacity.^[51] In this work, the helical ligament inspired by the configuration and deformation mechanism of the collagen fibers was introduced into a 3D chiral TTCM,^[11,17] and the highly coupled DOFs in the TTCM were removed to obtain the MP with TTCE.

The combination of stimulus-responsive materials (such as shape memory polymer, SMP) and 3D printing was employed, namely 4D printing.^[27–34] SMP was a kind of smart material that

X. Xin, L. Liu, Y. Liu
Department of Astronautical Science and Mechanics
Harbin Institute of Technology (HIT)
P.O. Box 301, No. 92 West Dazhi Street, Harbin 150001, P. R. China
E-mail: liulw@hit.edu.cn

J. Leng
Center for Composite Materials and Structures
Harbin Institute of Technology (HIT)
P.O. Box 3011, No. 2 Yikuang Street, Harbin 150080, P. R. China
E-mail: lengjs@hit.edu.cn

 The ORCID identification number(s) for the author(s) of this article can be found under <https://doi.org/10.1002/adfm.202107795>.

DOI: 10.1002/adfm.202107795

can maintain a temporary shape and recover to its original shape under environmental stimuli (such as thermal, magnetic, electrical, etc.).^[34] The 4D printing mechanical metamaterial combined the structural optimization design with the stimulus-response characteristics of the material, giving its programmable, reconfigurable, self-adaptive, and multifunctional characteristics, further enriching the mechanical properties of metamaterials.^[35–41]

In contrast to the mechanical properties of the existing TTCM that could only be adjusted by changing the geometric parameters of the microstructure, in this work the nonlinear mechanical properties of the MP with TTCE could be regulated by applying programming strain (ϵ_{target}), exhibiting programmability and reconfigurability.^[20–23] The feasibility of this bio-inspired strategy was proven through experimental tests, theoretical analysis, and finite element analysis (FEA), and the potential applications of the PMM for information encryptions, soft robots, and buffer devices were verified.

2. Results and Discussion

2.1. Design of the Metamaterials

The unit cell of the MP composed of a hollow cubic node and helical ligaments was obtained by removing the lateral

constraints of the 3D chiral TTCM with cubic symmetry (Figure 1A). The maximum torsion angle φ_{max} of the MP was increased by $\approx 438.10\%$ compared with the block structure before removing the constraint (Section S1, Supporting Information). The designed MP was chiral and non-centrosymmetric because it was not superimposed on its mirror image. The distribution of ligaments was divided into the right-handed chiral mode (Figure 1A) and the left-handed chiral mode (Figure 1A). The nodes were covered to eliminate the stress concentration, with a covering thickness of $L_m = 0.5$ mm (Section S2, Supporting Information). The centerline governing function of the helical ligament (Figure 1B) inspired by collagen fibers was $\mathbf{r} = R_\alpha \cos(\omega\vartheta) \sin\left(\frac{\vartheta}{2}\right) \mathbf{I}' + R_\alpha \sin(\omega\vartheta) \sin\left(\frac{\vartheta}{2}\right) \mathbf{J}' + \xi \frac{\vartheta}{2\pi} \mathbf{K}'$, where R_α , ω , and ξ represented the radius, the number of coils, and the distance between the two ends of the centerline, respectively. The MP (Figure 1C) was obtained by arranging n_p cells along the z -direction, and the φ increased with the increase of n_p (Section S3, Supporting Information). It was found that the chiral mode could regulate the torsion direction of the MP (Section S3, Supporting Information). When stretched along the z -direction, the φ direction of the MP with the right-handed chiral mode conformed to the left-handed rule, while the MP with the left-handed chiral mode showed the opposite torsion direction (Figure S5, Supporting Information). Interestingly,

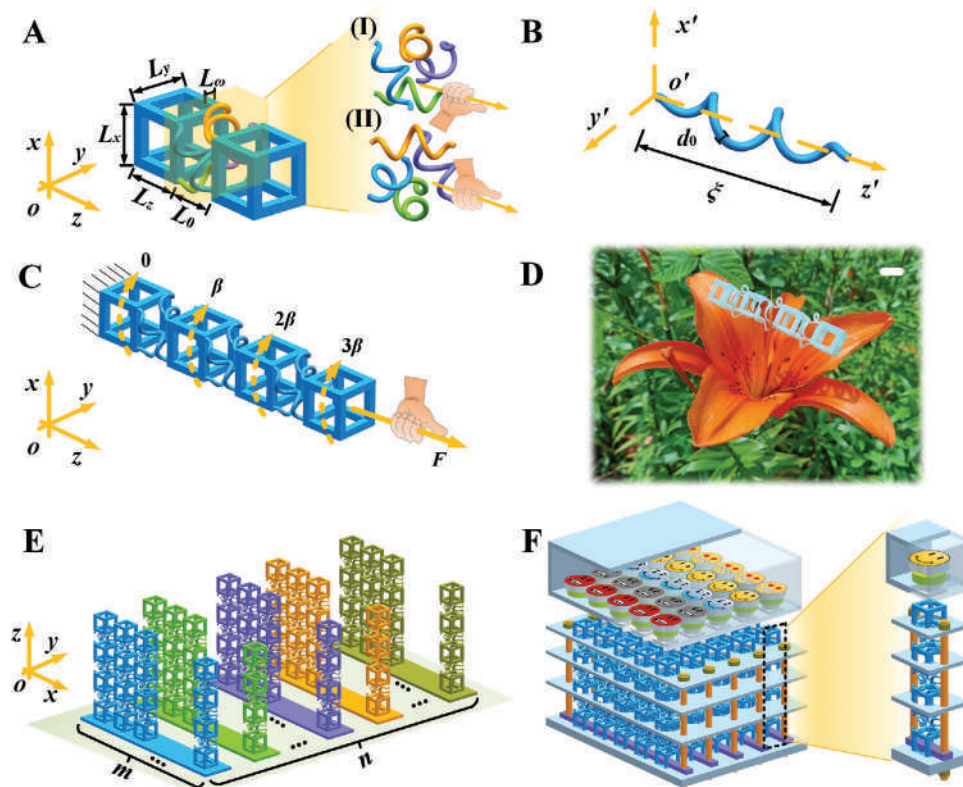


Figure 1. The CAD models of the MP and the PMM. A) The cell and geometric parameters of the TTCM. The connection mode of ligament and node can be divided into I) the right-handed mode and II) the left-handed mode. B) The helical microstructure inspired by collagen fibers. C) The deformation mechanism of the TTCM (i.e., the MP used in this work) with the right-handed chiral mode ($n_p = 3$). D) The lightweight of MP ($L_0/L_s = 0.9$, $R_\alpha/L_s = 0.3$, $\omega = 1$) allows it to be placed on the stamen. The scale bar is 10 mm. E) The schematic diagram of the PMM. F) A modular, programmable, and reconfigurable PMM is composed of several MPs with TTCE and a frame, ($m, n = (5, 5)$).

the printed MP had the characteristics of lightweight, and only the flower stamen can support its weight, Figure 1D.

The 8 dimensionless geometric parameters of the microstructure, including L_x/L_s , L_y/L_s , L_0/L_s , L_ω/L_s , R_α/L_s , d_0/L_s , ω , and n_p (where $L_s = L_z - 2L_m$), determined the mechanical properties and macroscopic configuration of the MP. L_x , L_y , L_z , and L_ω were the length, width, height, and thickness of the node. L_0 and d_0 represented the distance between adjacent nodes and the diameter of the ligaments, respectively. In this work, the effects of L_0/L_s (0.9, 1.4, 1.9), R_α/L_s (0.1, 0.2, 0.3, 0.4, 0.5), and ω (1, 2, 3, 4, 5, 6) on the mechanical properties of the MP were investigated (CAD models in Section-S3). By default, the MP had the right-handed chiral mode, $L_x/L_s = L_y/L_s = L_0/L_s = 1.1$, $L_\omega/L_s = 0.175$, $d_0/L_s = 0.1$, and $n_p = 3$.

Inspired by the array mode of hedgehog spines, the PMM was composed of (m, n) MPs with TTCE arrayed along with the (x, y) directions (Figure 1E) to eliminate the influence of lateral constraints on the TTCE. The MPs were connected with the bottom of a polymethyl methacrylate (PMMA) frame to improve the shear resistance of the PMM. Under a tensile load, the PMM was connected to a bearing section to release the torsional freedom of each MP (Figure 1F and Section S4, Supporting Information). The mechanical properties of the PMM were controlled with the configuration and arrangement of MPs, enabling the PMM to have diverse mechanical properties and modularization. It was worth noting that the TTCE of the MPs in the PMM remained unchanged because there was no connection between the MPs. Under external load, each MP in the PMM exhibited torsional deformation, which was different from the overall torsional deformation of the existing TTCM. The design strategy of the PMM increased the design freedom and configuration diversity of materials, while maintaining the TTCE of the MPs.

A laser cladding deposition 3D printer was employed to fabricate the MP with the photopolymerization of the photocurable polylactic acid-based SMP (PLA-based SMP) precursor solution. The glass transition temperature (T_g), Young's modulus, and elongation of the PLA-based SMP was ≈ 70.60 °C, ≈ 1.4 GPa, and $\approx 9\%$ (25 °C), respectively.^[6] The helical configuration allowed the MP to exhibit excellent deformability and TTCE (Movie S1, Supporting Information), and the shape memory effect (SME) of the MP allowed it to maintain a programmed temporary configuration and recover to its original configuration after reheating (Movie S2, Supporting Information).

2.2. Deformation Behavior Prediction of the MP with Infinitesimal Deformation

Since the mechanical properties of the MP depended on the geometric parameters of the microstructure, the relationship between the TTCE and the geometric parameters of the MP with infinitesimal deformation was derived.^[23,45–48] The micropolar theory, in contrast to the classical Cauchy theory, endowed each material point with six DOFs (i.e., displacement \mathbf{u} and rotation $\boldsymbol{\varphi}$). In addition to the conventional stress ($\boldsymbol{\sigma}$) and strain ($\boldsymbol{\varepsilon}$), the asymmetric higher-order stress (couple stress \mathbf{m}) and strain (curvature \mathbf{k}) were introduced into the micropolar theory.^[23] Therefore, the micropolar theory could describe the

rotation of the micropolar medium caused by chirality (Section S5, Supporting Information). The strain energy density of a micropolar medium could be described as:

$$w = \frac{1}{2} \varepsilon_{ij} C_{ijkl} \varepsilon_{kl} + \varepsilon_{ij} B_{ijkl} k_{kl} + \frac{1}{2} k_{ij} D_{ijkl} k_{kl} \quad (1)$$

where \mathbf{C} , \mathbf{B} , \mathbf{D} were fourth-order elastic tensors. In the Frenet framework, the stiffness matrix of the helical ligament in the local coordinate system ($o'-x'\gamma'z'$) was obtained through the balance equation and the law of kinematics (Figure 2A):^[47,48]

$$[K_e^{local}] = [T]^{-1} [K_e^{Frenet}] [T] \quad (2)$$

where, $[K_e^{local}]$ and $[K_e^{Frenet}]$ represented the stiffness matrix of the helical ligament in the $o'-x'\gamma'z'$ and the moving coordinate system $o-\tau n b$ (Figure S10B, Supporting Information), respectively. $[T]$ was the transformation matrix. The approximate relationship between the deformations of $O_{p,q,r}$ and $O_{p+1,q,r}$ was obtained with the Taylor expansion. The strain energy of the unit cell could be obtained:

$$w_{cell} = \frac{\sum_{i=1}^4 w_{ij}^i}{L_x L_y (L_z + L_0)} \quad (3)$$

where, w_{cell} and w_{ij} represented the strain energy of the cell and the ligament Ij , respectively. The material constants of the micropolar medium could be obtained:

$$C_{ijkl} = \frac{\partial^2 w_{cell}}{\partial \varepsilon_{ij} \partial \varepsilon_{kl}}, B_{ijkl} = \frac{\partial^2 w_{cell}}{\partial \varepsilon_{ij} \partial k_{kl}}, D_{ijkl} = \frac{\partial^2 w_{cell}}{\partial k_{ij} \partial k_{kl}} \quad (4)$$

The terms ε_{33} and k_{33} represented the displacement (w) and φ per unit length in the z-direction, respectively. The ratio k_{33}/ε_{33} represented the torsion accompanied by tension. Figure 2B,C and Figure S10, Supporting Information, display the results of the model and the FEA of k_{33}/ε_{33} for the MPs with different geometric parameters for infinitesimal deformation. k_{33}/ε_{33} achieved the tunability and designability by changing the geometric parameters of the MP, because the MPs with different configurations had different strain energies. In general, k_{33}/ε_{33} decreased with the increase of R_α and ω , and increased with the increase of L_0 , which was attributed to the untwisting deformation of the ligament of MP.

2.3. Nonlinear Behavior of the MP with Large Deformation

When the MP was applied to the tensile load, the tightly arranged helical ligaments gradually straightened, resulting in the nonlinear deformation of the MP transforming from the bending-dominated deformation mode to the stretching-dominated deformation mode. Figure 2D,E and Figure S11, Supporting Information, show the optical images and FEA results of the MPs under the tensile load. The helical ligament gradually untwisted and elongated, and the deformation mode of the MP was dominated by bending in the initial deformation process. The ligaments gradually paralleled the

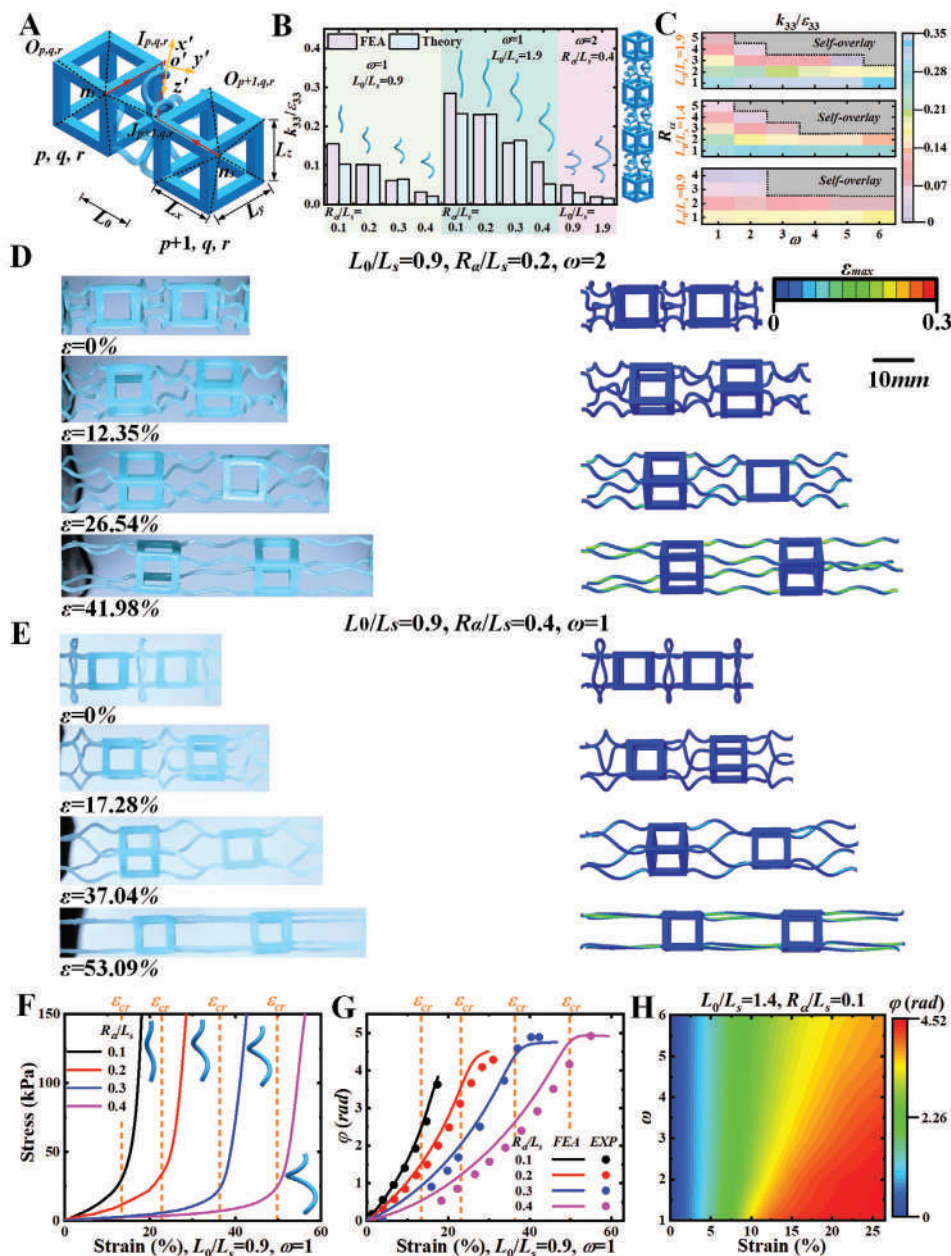


Figure 2. Deformation behavior analysis of the MP. A) The chiral lattice microstructure for homogenization. B) The model prediction and FEA comparison results of k_{33}/ϵ_{33} . C) The FEA results of k_{33}/ϵ_{33} . Comparison of experimental and FEM results of MPs with different ϵ : D) $L_0/L_s = 0.9$, $R_d/L_s = 0.2$, $\omega = 2$, and E) $L_0/L_s = 0.9$, $R_d/L_s = 0.4$, $\omega = 1$. F) σ - ϵ and G) φ - ϵ curves of the MPs with different geometric parameters. H) The FEA results of the influence of ω and ϵ on φ ($L_0/L_s = 1.4$, $R_d/L_s = 0.1$). The scale bar is 10 mm.

loading direction, which led to the torsion of the nodes. When the deformation exceeded the critical strain (ϵ_{cr}), the ligament was gradually straightened, and the deformation mode of the MP was dominated by stretching. For the deformation modes dominated by bending and stretching, the effective stiffness of the MP was determined by the second moment of the section and the cross-sectional area, respectively. The transformation of the deformation mode caused the MP to exhibit the J-shaped σ - ϵ curves, Figure 2F and Figure S12, Supporting Information. Interestingly, the helical ligament also increased

the deformability and flexibility of the MP, and the maximum deformation of the MP ($L_0/L_s = 1.4$, $R_d/L_s = 0.2$, $\omega = 4$) was ≈ 6.67 times that of the PLA-based SMP.

Figure 2G and Figure S13, Supporting Information show the FEA and experimental results of the φ - ϵ curves of the MPs with different geometric parameters, which were in good agreement. Figure 2H and Figure S14, Supporting Information, exhibit the contour plots of the influence of the microstructure parameters and ϵ on φ of the MP. The change of φ decreased gradually, as the MP transformed the deformation modes

dominated by stretching. When the helical ligament was completely straightened, the chiral behavior of the MP disappeared, and φ remained unchanged with the increase of ε . Furthermore, the maximum $\varphi_{\max}/\varepsilon$ of the MP ($L_0/L_s = 1.4$, $R_{\alpha}/L_s = 0.1$, $\omega = 1$) measured in this work was $\approx 0.35 \text{ rad } \%^{-1}$, which was increased by $\approx 902.68\%$ and $\approx 76.53\%$ compared with Refs. [20] and [26], respectively (Equation S29, Supporting Information).

Two kinds of helical ligaments with different geometric parameters were combined to adjust the nonlinear σ - ε of the MP for the condition of the similar φ - ε relationship, which greatly enriched the design freedom of the MP. For example, the helical ligaments with different geometric parameters were combined with ligament ($L_0/L_s = 0.9$, $R_{\alpha}/L_s = 0.1$, $\omega = 1$) to obtain MPs with different combinations, **Figure 3A,B** and **Figure S15**, Supporting Information. The adjustment range of the initial modulus of the combined MP was [61.97 kPa, 209.39 kPa], provided that the ratio φ/ε of the combined MP ($\approx 0.12 \text{ rad } \%^{-1}$) was similar. The reasons for this phenomenon were as follows: compared with other ligaments, the ligament ($L_0/L_s = 0.9$, $R_{\alpha}/L_s = 0.1$, $\omega = 1$) first entered the stretching-dominated deformation mode, thus the torsion effect of the combined MPs was determined by this ligament. The initial modulus of the combined MP was associated with each ligament, so it can be adjusted by changing the combined mode of the ligaments.

Besides, the J-shaped σ - ε relationship of the MPs could match that of biological tissues within the optimal deformation range ($\varepsilon \in [0\%, 40\%]$), such as skin and iliac artery (**Figure 3C**).^[42] The nonlinear mechanical behavior of the MPs could adapt to the deformation of tissues, showing the great potential of MPs in medical devices and wearable devices. The MP-based implants could reduce the tissue damage caused by the difference in the mechanical properties between implants and tissues.^[6,43]

2.4. The Programmability and the Reconfigurability of the Metamaterials

The dependence of the MP's mechanical properties on the geometric parameters created opportunities for the programmability and the reconfigurability of the MP's σ - ε and φ - ε curves. The implementation process was as follows: i) The MP was heated above T_g and stretched (ε_s), with the geometric parameters of the MP changing from L_x/L_s , L_y/L_s , L_0/L_s , L_{ω}/L_s , R_{α}/L_s , d_0/L_s , ω , and n_p to L_x/L_s , L_y/L_s , $(L_0/L_s)'$, L_{ω}/L_s , $(R_{\alpha}/L_s)'$, d_0/L_s , ω' , and n_p . ii) The MP could be fixed in this programmed configuration after cooling to room temperature and unloading. The geometric parameters of the programmed MP were changed from $(L_0/L_s)'$, $(R_{\alpha}/L_s)'$, ω' to $(L_0/L_s)''$, $(R_{\alpha}/L_s)''$, and ω'' because of partial elastic recovery (from ε_s to $\varepsilon_{\text{target}}$). Therefore, the programmed MP could be a new MP with different mechanical properties to bear the external load. iii) When reheated ($>T_g$), the configuration and the mechanical properties of the programmed MP recovered to their original states. The precise programming of the PMM can be realized by assembling the MP with the programmed configuration into the PMM frame. Since there was no interconnection between MPs, each MP in the PMM can be programmed to different configurations.

Figure 3D–F, **Figures S16** and **S17**, Supporting Information, show the programmability of the nonlinear mechanical properties (σ - ε and φ - ε curves) of the MP. Importantly, the nonlinear mechanical properties of the 4D printing MP could be adjusted not only by changing the geometry parameters of the microstructure but also by applying $\varepsilon_{\text{target}}$. For example, when $\varepsilon_{\text{target}}$ was 21.13% and 33.80%, the σ - ε curve of the programmed MP ($L_0/L_s = 0.9$, $R_{\alpha}/L_s = 0.4$, $\omega = 1$) could match those of the MP ($L_0/L_s = 0.9$, $R_{\alpha}/L_s = 0.2$, $\omega = 1$) and MP ($L_0/L_s = 0.9$, $R_{\alpha}/L_s = 0.1$, $\omega = 1$), respectively. In the above two $\varepsilon_{\text{target}}$, the φ - ε curves of the programmed MP ($L_0/L_s = 0.9$, $R_{\alpha}/L_s = 0.4$, $\omega = 1$) could match those of the MP ($L_0/L_s = 0.9$, $R_{\alpha}/L_s = 0.3$, $\omega = 1$) and MP ($L_0/L_s = 0.9$, $R_{\alpha}/L_s = 0.1$, $\omega = 2$), respectively.

2.5. Application Prospects

The PMM eliminated the internal coupling constraints of the bulk structures and greatly released the deformation potential. The programmability of the MP and the modular design significantly enriched the diversity configuration and the mechanical properties of the PMM. **Figure 3G**, **Figure S9**, and **Movie S3**, Supporting Information, show a PMM consisting of $(m, n) = (5, 5)$ MPs. The torsion of each pixel could be designed by adjusting the parameters and the chiral mode of the MP.

The application prospect of the PMM $(m, n) = (5, 3)$ in information encryption is demonstrated by the programmability of the MPs with different chiral modes in the PMM, **Figure 3H**, **Figure S18**, and **Movie S4**, Supporting Information. When the PMM was heated and mechanically deformed, the torsion of the MPs enabled the image to be displayed as an "H", and the PMM could be fixed in this decrypted state after cooling. Then the PMM was reheated, and the image recovered to the encrypted state. More importantly, this encryption method could be extended to the endless encrypted image set and the 2D code encryption.^[44]

In addition, the developed PMM also showed promising application potential for kinematics controllers, soft robots, and buffer devices.

Figure 4A and **Movie S5**, Supporting Information, show that the PMM $(m, n) = (1, 1)$ with the right-handed chiral mode could control the football ($\approx 13.38 \text{ g}$) to produce different movements by applying tension/compression deformation. The PMM with the left-handed chiral mode, in contrast, could produce the opposite movement from that of the PMM with the right-handed chiral mode, **Figure S19**, Supporting Information.

The egg ($\approx 68.22 \text{ g}$) was placed on the PMM $(m, n) = (5, 5)$, and the geometric parameters of the MPs were $L_0/L_s = 0.9$, $R_{\alpha}/L_s = 0.2$, and $\omega = 1$. Because of the configuration of the helical ligaments, the PMM allowed a load of $\approx 32 \text{ N}$ (31.84 N) to be applied to the egg within the deformation range of 10.55 mm, **Figure 4B,C** and **Movie S6**, Supporting Information. The collaborative deformation process of the egg and the PMM exhibited a J-shaped force-displacement curve, indicating that large deformation can be generated under small force, showing the superiority of the PMM in soft robots. Specifically, this large range of protective displacements could be converted into very comfortable tolerances and soft contacts to control the motion of the robotic arm.^[19] In addition, soft-touch in robotic surgery can play a protective role to significantly reduce tissue invasion.

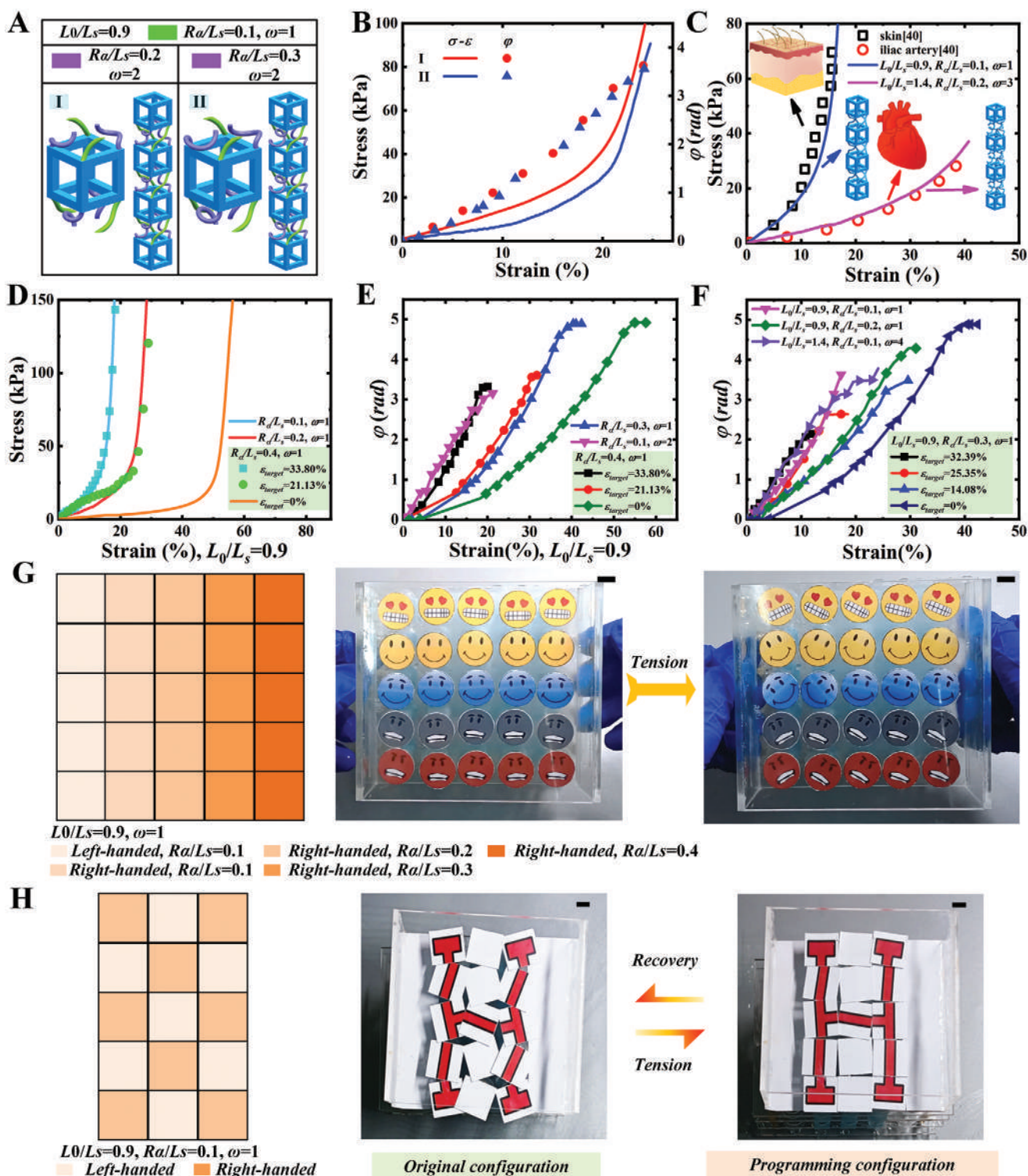


Figure 3. The programmability of the MP and application demonstration of the PMM. A,B) The combined microstructure with different ligaments can adjust the stiffness of the MP. C) The J-shaped $\sigma-\varepsilon$ curve of the MP can match skin and iliac artery within the optimal deformation range ($\varepsilon \in [0, 40\%]$). The programmability of D) the $\sigma-\varepsilon$ and E,F) $\varphi-\varepsilon$ curves of the MP. G) The PMM assembled by the MPs with different geometric parameters can control the rotation angle under a tensile load, $(m, n) = (5, 5)$. H) The information is encrypted and decrypted through the programmability of the PMM, $(m, n) = (5, 3)$. The scale bar is 10 mm.

A *Right-handed chiral mode*

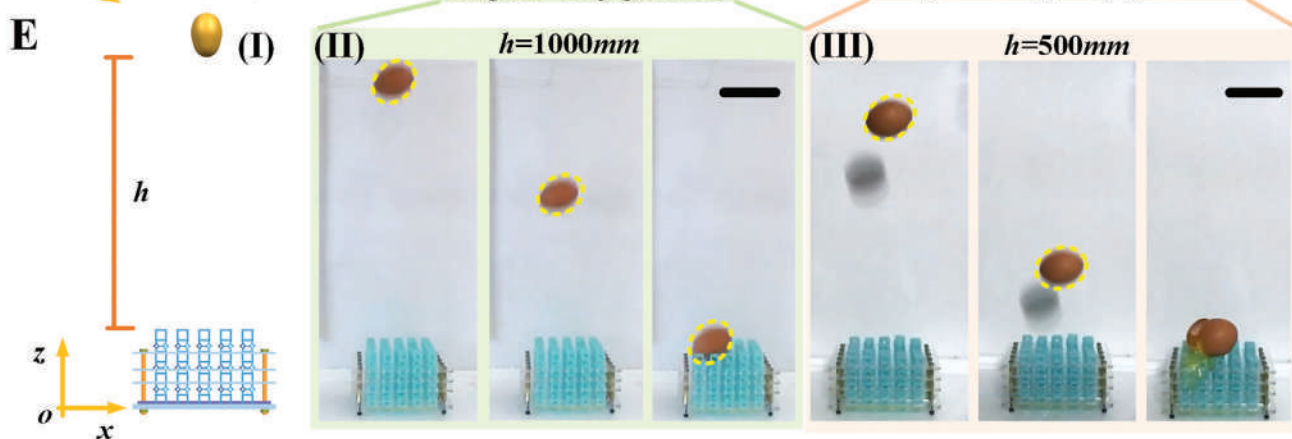
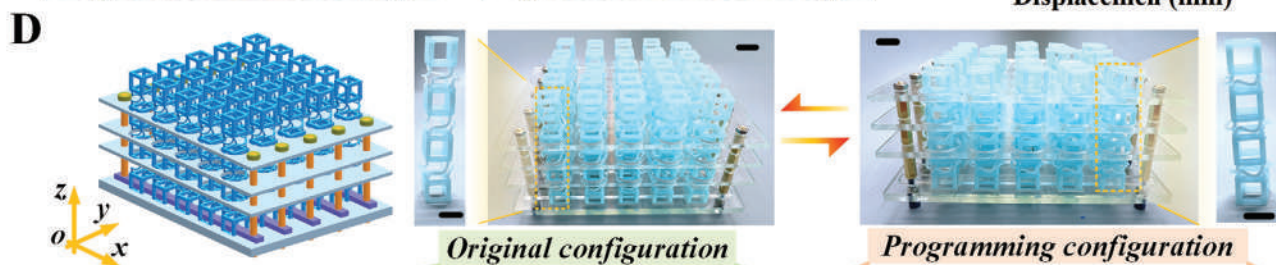
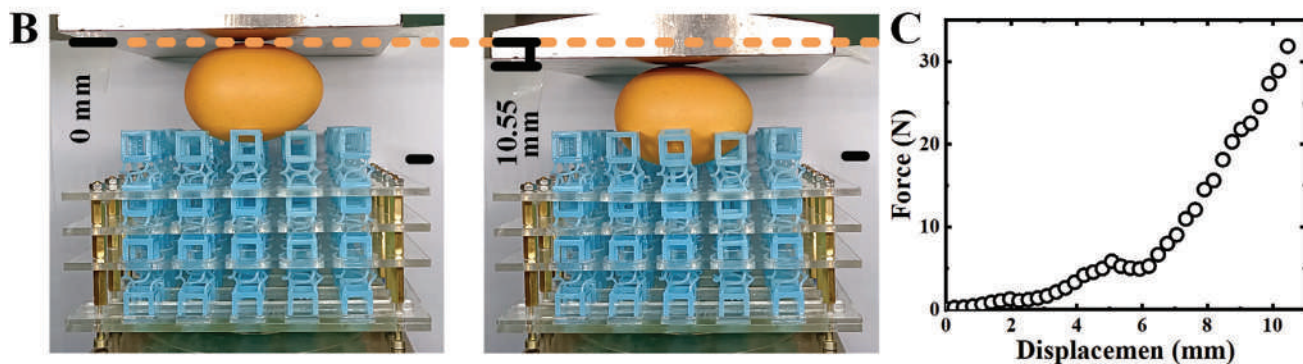
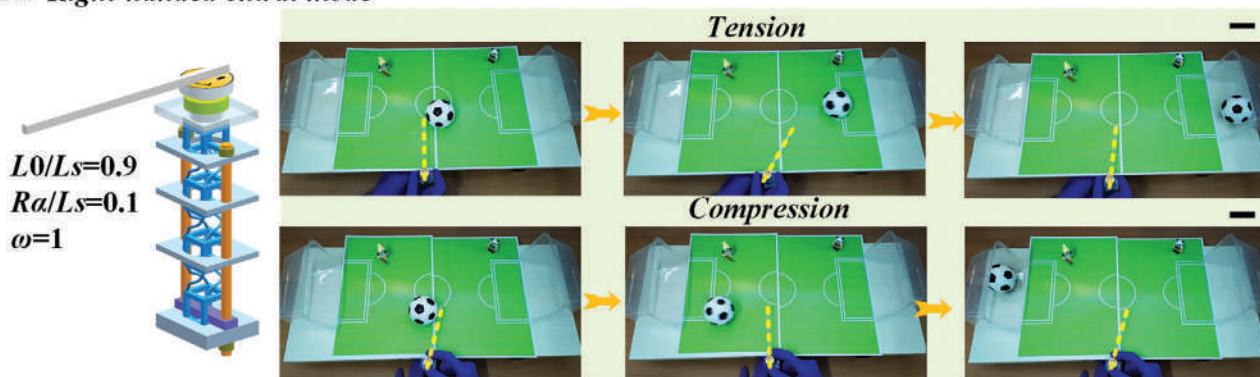


Figure 4. The potential application demonstrations of the PMM. A) The PMM with the right-handed mode can control the football to produce different motion modes under tension and compression loads. The scale bar is 50 mm. The PMM can protect eggs from damage under the compression load: B) optical images and C) the load–displacement curve. The scale bar is 10 mm. D) The PMM before and after programming ($\epsilon_{\text{target}} = -14.79\%$). The scale bar is 10 mm. E) The dynamic impact experiment of free-falling eggs on the PMM: I) CAD model. II) The egg falls freely onto the unprogrammed PMM ($h = 1000$ mm). III) The egg falls freely onto the programmed PMM ($h = 500$ mm). The scale bar is 100 mm.

In addition, the PMM exhibited promising prospects to be developed into buffer devices through a variety of protection mechanisms. Among the various mechanisms, the helical ligament deformation was the dominant mechanism of the PMM. During compression/impact, the large L_0/L_s allowed the ligament to deform in a large enough space, thus providing sufficient buffer for the fragile objects (such as eggs). Therefore, the programmability of the PMM allowed the protection performance of the PMM to be adjusted by changing the configuration of the MPs, such as L_0/L_s . Compared with the PMM composed of MPs with multi-stable effect,^[25] the PMM designed in this work exhibited lower stiffness and had no force threshold for activating the protection mechanism, demonstrating the ability to protect more fragile objects. The main protection mechanism of PMM based on multi-stable MPs was the negative stiffness characteristic caused by the structural configuration. There was a force threshold to activate the negative stiffness characteristic. Before reaching this threshold, the force-displacement curve of the MP with multi-stable property exhibited a linearly increasing trend. This may not provide an effective protection for fragile objects because the object may have been damaged before this threshold is reached.

The buffer device was obtained by the PMM ($(L_0/L_s = 0.9, R_{\alpha}/L_s = 0.2, \omega = 1, (m, n) = (5, 5))$, Figure 4D). The MPs in the PMM were precisely programmed ($\epsilon_{\text{target}} = -14.79\%$) to adjust the protection performance of the PMM, Figure 4D). The dynamic impact experiments of the eggs freely falling from different heights ($h = 500$ and 1000 mm) to the PMM before and after programming were demonstrated, which visually verified the protection ability and programmability of the PMM (Figure 4E, Figure S20, and Movie S7, Supporting Information). The egg fell from a height of 1000 mm on the PMM and remained intact, while the egg broke immediately when it fell from 500 mm to the programmed PMM. The geometric parameters and the arrangement of the MP could be adjusted according to the specific protected object. More importantly, the modular design enabled the PMM to be quickly rebuilt and repaired after being impacted, even if its constituent unit (MP) was damaged, demonstrating the maintainability of the material. The PMM provided new options for the design of reusable buffer materials such as personnel protection.

3. Conclusion

In summary, a novel strategy was proposed to address the limitations of the weak TTCE, small strain range, and weak adaptive ability of the TTCM by combining the helical ligament, MP array design, and 4D printing. The maximum $\phi_{\text{max}}/\epsilon$ of the developed MP with TTCE was ≈ 0.35 rad $\%^{-1}$, which was increased by $\approx 902.68\%$ and $\approx 76.53\%$ compared with the previous reports Refs. [20] and [26]. The maximum deformation of the MP was $\approx 60.91\%$, which was ≈ 6.67 times that of PLA-based SMP. The relationship between the mechanical properties and the geometric parameters of the MP was investigated through

theoretical analysis, FEA and experiments. The combined microstructures with different geometric parameters were employed to adjust the effective stiffness of the metamaterials for the specific TTCE. The programmability and reconfigurability characteristics of the SMP-based MPs were determined using the quantitative relationship between the mechanical properties and ϵ . The modularity of the PMM assembled with 4D printed MP greatly increased the design freedom and the diversity of the mechanical properties of the metamaterials. Furthermore, the PMMs showed immense potential for information encryptions, kinematics controllers, soft robots, and buffer devices.

4. Experimental Section

Design and Fabrication of Metamaterials: The CAD models of MPs and PMMs were built with UG NX (Siemens) software, and the cross-section images of the models were extracted with Photon Workshop. The LED wavelength of the LCD printer and the accuracies of the X/Y axis and the Z axis were 405 nm, 0.047 mm, and 0.00125 mm, respectively.

Experimental Method: The nonlinear behavior of the metamaterials was investigated with a Zwick-010 tensile machine with an environmental chamber at a rate of 5 mm min^{-1} . During the test, the deformation processes of the metamaterial were recorded with a camera (Canon ds126571). The normal mode (1080 p and 30 fps) and the slow-motion mode (720 p and 240 fps) of the camera were used to capture the egg falling process.

Finite Element Analyses: The software ABAQUS/Standard (SIMULIA) was employed to establish the finite element model and simulate the nonlinear deformation behavior of the MP. A 10-node quadratic tetrahedron (C3D10) element was used to mesh the MP. The mechanical parameters of PLA-based SMP have been detailed in the previous work.^[6] The reference points (RPs) were added to the upper and lower surfaces along the longitudinal direction of the MP and coupled with the upper and lower surfaces. The boundary conditions of the RPs coupled to the upper and lower surfaces were $U_1 = U_2 = UR_1 = UR_2 = 0$ and ENCASTRE ($U_1 = U_2 = U_3 = UR_1 = UR_2 = UR_3 = 0$), respectively. The displacement along the z direction (U_3) was applied to the RP coupled with the upper surface.

Supporting Information

Supporting Information is available from the Wiley Online Library or from the author.

Acknowledgements

The authors gratefully acknowledge the financial supports provided by the National Natural Science Foundation of China (Grant Nos. 12172106, 11632005, 12072094, and 11672086).

Conflict of Interest

The authors declare no conflict of interest.

Data Availability Statement

Research data are not shared.

Keywords

4D printing, pixel mechanical metamaterials, shape memory polymers, tension-torsion coupling metamaterials

Received: August 7, 2021
Revised: October 1, 2021
Published online:

-
- [1] T. Chen, M. Pauly, P. M. Reis, *Nature* **2021**, 589, 386.
- [2] A. Clausen, F. Wang, J. S. Jensen, O. Sigmund, J. A. Lewis, *Adv. Mater.* **2015**, 27, 5523.
- [3] S. C. Shan, S. H. Kang, J. R. Raney, P. Wang, L. C. Fang, F. Candido, J. A. Lewis, K. Bertoldi, *Adv. Mater.* **2015**, 27, 4296.
- [4] S. Janbaz, K. Narooei, T. van Manen, A. A. Zadpoor, *Sci. Adv.* **2020**, 6, eaba0616.
- [5] X. G. Guo, X. Y. Ni, J. H. Li, H. Zhang, F. Zhang, H. B. Yu, J. Wu, Y. Bai, H. S. Lei, Y. G. Huang, J. A. Rogers, Y. H. Zhang, *Adv. Mater.* **2021**, 33, 2004919.
- [6] X. Z. Xin, L. W. Liu, Y. J. Liu, J. S. Leng, *Adv. Funct. Mater.* **2020**, 30, 2004226.
- [7] B. L. Deng, S. Q. Yu, A. E. Forte, V. Tournat, K. Bertoldi, *Proc. Natl. Acad. Sci. USA* **2020**, 117, 31002.
- [8] K. Bertoldi, V. Vitelli, J. Christensen, M. van Hecke, *Nat. Rev. Mater.* **2017**, 2, 17066.
- [9] J. X. Liu, D. J. Yan, Y. H. Zhang, *J. Mech. Phys. Solids* **2021**, 146, 104210.
- [10] V. Hahn, P. Kiefer, T. Frenzel, J. Y. Qu, E. Blasco, C. Barner-Kowollik, M. Wegener, *Adv. Funct. Mater.* **2020**, 30, 1907795.
- [11] H. Zhang, X. G. Guo, J. Wu, D. N. Fang, Y. H. Zhang, *Sci. Adv.* **2018**, 4, eaar8535.
- [12] X. Y. Ni, X. G. Guo, J. H. Li, Y. G. Huang, Y. H. Zhang, J. A. Rogers, *Adv. Mater.* **2019**, 31, 1905405.
- [13] A. Papadopolou, J. Laucks, S. Tibbits, *Nat. Rev. Mater.* **2017**, 2, 17078.
- [14] H. Zhang, J. Wu, D. N. Fang, Y. H. Zhang, *Sci. Adv.* **2021**, 7, eabf1966.
- [15] D. Melancon, B. Gorissen, C. J. Garcia-Mora, C. Hoberman, K. Bertoldi, *Nature* **2021**, 592, 545.
- [16] J. H. Shi, H. Mofatteh, A. Mirabolghasemi, G. Desharnais, A. Akbarzadeh, *Adv. Mater.* **2021**, 33, 2102423.
- [17] D. J. Yan, J. H. Chang, H. Zhang, J. X. Liu, H. L. Song, Z. G. Xue, F. Zhang, Y. H. Zhang, *Nat. Commun.* **2020**, 11, 1180.
- [18] J. Liu, Y. Zhang, *Soft Matter* **2018**, 14, 693.
- [19] S. Janbaz, F. S. L. Bobbert, M. J. Mirzaali, A. A. Zadpoor, *Mater. Horiz.* **2019**, 6, 1138.
- [20] T. Frenzel, M. Kadic, M. Wegener, *Science* **2017**, 358, 1072.
- [21] Y. Chen, T. Frenzel, S. Guenneau, M. Kadic, M. Wegener, *J. Mech. Phys. Solids* **2020**, 137, 103877.
- [22] R. Tao, L. T. Ji, Y. Li, Z. S. Wan, W. X. Hu, W. W. Wu, B. B. Liao, L. H. Ma, D. N. Fang, *Composites, Part B* **2020**, 201, 108344.
- [23] S. Y. Duan, W. B. Wen, D. N. Fang, *J. Mech. Phys. Solids* **2018**, 121, 23.
- [24] L. Meng, J. X. Shi, C. Yang, T. Gao, Y. L. Hou, L. L. Song, D. D. Gu, J. H. Zhu, P. Breitkopf, W. H. Zhang, *Extreme. Mech. Lett.* **2020**, 40, 100869.
- [25] F. Pan, Y. L. Li, Z. Y. Li, J. L. Yang, B. Liu, Y. L. Chen, *Adv. Mater.* **2019**, 31, 1900548.
- [26] B. B. Zheng, R. C. Zhong, X. Chen, M. H. Fu, L. L. Hu, *Mater Design* **2019**, 171, 107700.
- [27] C. Lin, J. X. Lv, Y. S. Li, F. H. Zhang, J. R. Li, Y. J. Liu, L. W. Liu, J. S. Leng, *Adv. Funct. Mater.* **2019**, 29, 1906569.
- [28] W. Zhang, H. Wang, H. Wang, J. Y. E. Chan, H. Liu, B. Zhang, Y. F. Zhang, K. Agarwal, X. Yang, A. S. Ranganath, H. Y. Low, Q. Ge, J. K. W. Yang, *Nat. Commun.* **2021**, 12, 112.
- [29] M. O. Saed, C. P. Ambulo, H. Kim, R. De, V. Raval, K. Searles, D. A. Siddiqui, J. M. O. Cue, M. C. Stefan, M. R. Shankar, T. H. Ware, *Adv. Funct. Mater.* **2019**, 29, 1806412.
- [30] X. Kuang, D. J. Roach, J. T. Wu, C. M. Hamel, Z. Ding, T. J. Wang, M. L. Dunn, H. J. Qi, *Adv. Funct. Mater.* **2019**, 29, 1805290.
- [31] L. M. Huang, R. Q. Jiang, J. J. Wu, J. Z. Song, H. Bai, B. G. Li, Q. Zhao, T. Xie, *Adv. Mater.* **2017**, 29, 1605390.
- [32] M. Falahati, P. Ahmadvand, S. Safaee, Y. C. Chang, Z. Y. Lyu, R. Chen, L. Li, Y. H. Lin, *Mater. Today* **2020**, 40, 215.
- [33] Q. J. Ze, X. Kuang, S. Wu, J. Wong, S. M. Montgomery, R. D. Zhang, J. M. Kovitz, F. Y. Yang, H. J. Qi, R. K. Zhao, *Adv. Mater.* **2020**, 32, 1906657.
- [34] Y. L. Xia, Y. He, F. H. Zhang, Y. J. Liu, J. S. Leng, *Adv. Mater.* **2021**, 33, 2000713.
- [35] W. Hu, Z. Ren, Z. Wan, D. Qi, X. Cao, Z. Li, W. Wu, R. Tao, Y. Li, *Mater Design* **2021**, 200, 109481.
- [36] R. Tao, L. Xi, W. W. Wu, Y. Li, B. B. Liao, L. W. Liu, J. S. Leng, D. N. Fang, *Compos. Struct.* **2020**, 252, 112663.
- [37] Z. W. Ren, L. T. Ji, R. Tao, M. J. Chen, Z. S. Wan, Z. Zhao, D. N. Fang, *Extreme Mech Lett* **2021**, 42, 101077.
- [38] S. Li, B. Deng, A. Grinthal, A. Schneider-Yamamura, J. Kang, R. S. Martens, C. T. Zhang, J. Li, S. Yu, K. Bertoldi, J. Aizenberg, *Nature* **2021**, 592, 386.
- [39] C. Yang, M. Boorugu, A. Dopp, J. Ren, R. Martin, D. Han, W. Choi, H. Lee, *Mater. Horiz.* **2019**, 6, 1244.
- [40] D. Wang, H. P. Xu, J. Q. Wang, C. R. Jiang, X. Y. Zhu, Q. Ge, G. Y. Gu, *ACS Appl. Mater. Interfaces* **2020**, 12, 22146.
- [41] Z. A. Zhao, C. Yuan, M. Lei, L. Yang, Q. Zhang, H. S. Chen, H. J. Qi, D. N. Fang, *Phys. Rev. Appl.* **2019**, 11, 044074.
- [42] S. S. Sheiko, A. V. Dobrynin, *Macromolecules* **2019**, 52, 7531.
- [43] C. Lin, L. Liu, Y. Liu, J. Leng, *ACS Appl. Mater. Interfaces* **2021**, 13, 12668.
- [44] N. An, A. G. Domel, J. X. Zhou, A. Rafsanjani, K. Bertoldi, *Adv. Funct. Mater.* **2020**, 30, 1906711.
- [45] X. N. Liu, G. L. Huang, G. K. Hu, *J. Mech. Phys. Solids* **2012**, 60, 1907.
- [46] Y. Chen, X. N. Liu, G. K. Hu, Q. P. Sun, Q. S. Zheng, *Proc. R. Soc. A* **2014**, 470, 20130734.
- [47] F. N. Gimena, P. Gonzaga, L. Gimena, *Eng Struct* **2008**, 30, 1770.
- [48] V. Haktanir, E. Kiral, *Comput. Struct.* **1993**, 49, 663.
- [49] N. B. Swift, B.-K. Hsiung, E. B. Kennedy, K.-T. Tan, *J. Mech. Behav. Biomed. Mater.* **2016**, 61, 271.
- [50] J. F. Vincent, P. Owers, *J. Zool.* **1986**, 210, 55.
- [51] J. X. Liu, D. J. Yan, W. B. Pang, Y. H. Zhang, *Mater. Today* **2021**, <https://doi.org/10.1016/j.mattod.2021.05.007>.